Semi-analytical response of acoustic logging measurements in frequency domain

Ignacio Muga

Instituto de Matemáticas, Pontificia Universidad Católica de Valparaíso, Casilla 4059, Valparaíso, Chile

David Pardo

Department of Applied Mathematics, Statistics and Operational Research, University of the Basque Country (UPV/EHU), BCAM (Basque Center for Applied Mathematics) and IKERBASQUE (Basque Foundation for Sciences), Bilbao, Spain

Paweł J. Matuszyk

Department of Petroleum & Geosystems Engineering, The University of Texas at Austin, 1 University Station C0300, Austin, TX 78712-0228, USA
currently Baker Hughes Inc., Houston, USA

Carlos Torres-Verdín

Department of Petroleum & Geosystems Engineering, The University of Texas at Austin, 1 University Station C0300, Austin, TX 78712-0228, USA

Abstract

This work proposes a semi-analytical method for simulation of the acoustic response of multipole eccentered sources in a fluid-filled borehole. Assuming a geometry that is invariant with respect to the azimuthal and vertical directions, the solution in frequency domain is expressed in terms of a Fourier series and a Fourier integral. The proposed semi-analytical method builds upon the idea of separating singularities from the smooth part of the integrand when performing the inverse Fourier transform. The singular part is treated analytically using existing inversion formulae, while the regular

Email addresses: `ignacio.muga@ucv.cl` (Ignacio Muga), `dzubiaur@gmail.com` (David Pardo), `pawel@ices.utexas.edu` (Paweł J. Matuszyk), `cverdin@uts.cc.utexas.edu` (Carlos Torres-Verdín)

part is treated with a FFT technique. As a result, a simple and effective method that can be used for simulating and understanding the main physical principles occurring in borehole-eccentered sonic measurements is obtained. Numerical results verify the proposed method and illustrate its advantages.

1. Introduction

Sonic logging instruments are routinely used to asses the main mechanical properties of the subsurface, enabling estimation of the amount and type of hydrocarbons present in a reservoir. However, in actual borehole logging conditions, sonic logging measurements are often difficult to interpret, and they may produce a miscalculation in the hydrocarbon estimation. A well-known situation in which sonic measurements are challenging to interpret is when the logging instrument is located at a nonzero distance from the center of the borehole, the so-called *borehole-eccentered* measurements (cf. [1, 2]). To facilitate interpretation of borehole-eccentered measurements, it is necessary to develop effective numerical simulation methods in frequency domain, which provide direct information about the dispersion and velocities of the wave propagation phenomena.

The numerical codes developed for this purpose — most of them based in finite-element discretizations — need to be constantly improved and verified. A powerful and simple test is to benchmark these codes with results that can be obtained by a completely different method, the latter being as analytical as possible. Analytical codes are also used to postprocess in real-time acquired sonic waveforms, which enable corrections on the trajectory of the so-called logging-while-drilling (LWD) instruments.

A simple way to obtain analytical representations of solutions is to assume geometric invariance in two of the three spatial dimensions. Here, we assume a concentric borehole model where the vertical and azimuthal directions remain invariant. In this case, the wavefield produced by a (time-harmonic) point source can be represented by an inverse Fourier integral in terms of the axial coordinate, and a Fourier series in terms of the azimuthal coordinate (cf. [3]). The main computational difficulty is to deal with the singularities of the integrand function in the Fourier inversion, which makes imposible

a direct application of a FFT technique or any other conventional numerical integration method. Indeed, those singularities are not integrable in the classical (L^1 or Riemann) sense. Therefore, the Fourier inversion only has a meaning in a *distributional sense*. So far, two numerical techniques have been used to compute this last Fourier inversion integral. One technique is known as the *real axis integration* (RAI) method, introduced by Rosenbaum [4] and Tsang & Rader [5]. The other technique employs a deformed integration path in the complex plane and the most common reference to this method is the work of Kurkjian [6].

The RAI method [5, 7] is conceptually easy to apply, but it is a method adapted to recover the solution in time-domain rather than in frequency-domain. Basically, by adding a sufficiently large imaginary part in the frequency variable, the singularities of the integrand function are shifted away from the real axis towards the complex plane. This allows to perform a direct integration over the real axis with a FFT technique, at the expense of introducing a solution defined over a complex path of the frequency domain rather than the traditional real frequency domain space. This prevents us from directly studying frequency domain features that are routinely analyzed in borehole acoustics. For that purpose, one would need to perform additional Fourier transforms, which can be cumbersome and prone to numerical errors. Nonetheless, the RAI method can be applied to several logging scenarios (see [8] or [9]).

On the other hand, the method that uses Cauchy theory [6] is well adapted to recover the frequency-domain solution, but it can be difficult to handle because it involves several integrals in the complex plane. Basically, the Fourier inversion integral is computed as the sum of residues given by the singularities, plus integrals over both sides of the brunch cuts where the integrated function is non-analytic. A slight modification to this technique, in which the residues are computed using a Laurent series expansion, can be found in the recent article [10].

In this paper we use a different approach, which is at the same time conceptually simple and adapted to recover the frequency-domain solution. Since the integrand has non-integrable singularities, it must be regarded as *a tempered distribution* (the space of distributions where the Fourier transform is well-defined). Then, by isolating the singularities, we split the integrated function into a non-integrable part (but still a tempered distribution) plus an integrable part in the $L^1(\mathbb{R})$ sense. The non-integrable part is treated analytically using conventional Fourier transform formulae, while the inte-

3

grable part is treated numerically with a FFT technique over the real axis (no complex integration paths are used). The idea of decomposing the inverse Fourier transform into analytic and numeric counterparts is widely used in many communities, particularly when evaluating Green's functions for applications in electrical engineering, mechanical engineering, geophysics and boundary elements (cf. [11, 12, 13, 14]). Our case is particularly challenging because the map of singularities is complicated: we have several of them, each one depends nonlinearly upon the frequency, and most of them have cut-off frequencies.

We apply this approach to compute the (time-harmonic) acoustic response of a fluid-filled borehole due to multipole eccentered excitations, including some extreme situations where the sources are very close to the borehole wall. We verify our technique against the classical results of Kurkjian [6] and the latest finite-element approach proposed in [1].

This paper is organized as follows. First, we describe the model problem to be solved. Then, we derive the mathematical formulation of our semi-analytical method. Finally, we present some benchmarks and challenging numerical results followed by the main conclusions. This paper also contains an appendix that describes explicitly the radial stress in Fourier domain.

2. Model problem

Using cylindrical coordinates (r, θ, z), we consider a fluid with sound velocity $c_f > 0$ and density $\rho_f > 0$ filling the borehole $\Omega_f := \{(r, \theta, z) : r < R\}$. An isotropic elastic solid of density $\rho_s > 0$ and Lamé coefficients $\lambda, \mu > 0$ is surrounding the borehole in a region $\Omega_s := \{(r, \theta, z) : r > R\}$. The domains are invariant under rotation and translation in the z-direction. We want to analyze the pressure response in the fluid, due to a time-harmonic point source excitation. Single point source is characterized by its angular frequency $\omega > 0$ and placed for convenience at $(r_s, 0, 0)$, where $0 < r_s < R$ (see Fig. 1). More complicated types of sources like eccentered monopoles, dipoles or quadrupoles are obtained by a simple superposition technique (see Section 3.4 or cf. [15]).

The characteristic wavenumbers are denoted by $k_f = \omega/c_f$ for the fluid, and $k_p = \omega(\rho_s/(\lambda + 2\mu))^{1/2}$ together with $k_s = \omega(\rho_s/\mu)^{1/2}$ for the compressional and shear wavenumber of the solid, respectively.

The pressure response in the fluid and the displacement field response in the elastic solid are represented by $p = p(r, \theta, z; \omega)$ and $\boldsymbol{u} = \boldsymbol{u}(r, \theta, z; \omega) =$
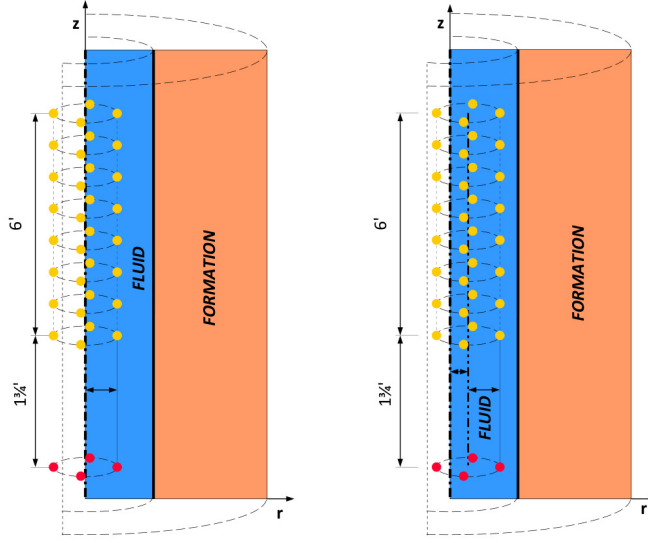
Figure 1: Typical geometry for problems with one acoustic source composed of four excitation points (red points) and an array of eight receivers (yellow points). Left: centered model. Right: eccentered model.

$u_r \boldsymbol{e}_r + u_\theta \boldsymbol{e}_\theta + u_z \boldsymbol{e}_z$, respectively, where $\{\boldsymbol{e}_r, \boldsymbol{e}_\theta, \boldsymbol{e}_z\}$ denotes the set of canonical vectors in cylindrical coordinates. The corresponding set of partial derivatives is denoted by $\{\partial_r, \partial_\theta, \partial_z\}$.

Given an amplitude $A \in \mathbb{C}$ of the source, the pressure behavior in fluid domain is governed by the Helmholtz equation:

$$
\begin{cases}
\Delta p + k_f^2 p & = -\dfrac{A}{r}\delta(r - r_s)\delta(\theta)\delta(z) \quad \text{in } \Omega_f \,, \\
\partial_r p & = \rho_f \omega^2 u_r \qquad\qquad\qquad\quad \text{over } r = R \,,
\end{cases}
\tag{1}
$$

where the symbol δ stands for the Dirac delta distribution, and the scalar Laplacian in cylindrical coordinates is given by:

$$
\Delta = \frac{1}{r}\,\partial_r(r\partial_r) + \frac{1}{r^2}\,\partial_\theta^2 + \partial_z^2 \,.
$$

The linear elastodynamic equations governing the displacement field in the solid are:

$$
\begin{cases}
\boldsymbol{u} + \dfrac{1}{k_p^2}\nabla\nabla \cdot \boldsymbol{u} - \dfrac{1}{k_s^2}\nabla \times \nabla \times \boldsymbol{u} & = \boldsymbol{0} \qquad\quad \text{in } \Omega_s \,, \\
\boldsymbol{\sigma}(\boldsymbol{u})\boldsymbol{e}_r & = -p\boldsymbol{e}_r \quad \text{over } r = R \,,
\end{cases}
\tag{2}
$$

5

where $\boldsymbol{\sigma}$ stands for the Cauchy stress tensor in cylindrical coordinates (cf. [16]).

3. Derivation of the semi-analytical method

3.1. The spectral solutions

In this section, equations (1) and (2) will be transformed via classical Fourier transform in the geometrical invariant variables (θ, z), i.e.,

$$\widehat{v}_n(\xi) = \frac{1}{2\pi} \int_{(-\pi,\pi)\times\mathbb{R}} v(\theta, z) \cos(n\theta) e^{i\xi z} d\theta dz.$$

The solutions of the transformed equations, which depend now on wavenumber variable ξ and azimuthal order n (as well as on the observation radius r, the source radius r_s, and the angular frequency ω), will be called *the spectral solutions*.

The inverse Fourier transform will be defined as:

$$v(\theta, z) = \sum_{n=0}^{+\infty} \frac{\epsilon_n}{2\pi} \int_{\mathbb{R}} \widehat{v}_n(\xi) e^{-i\xi z} d\xi \cos(n\theta), \quad \text{where } \epsilon_n = \left\{ \begin{array}{ll} 1 & \text{if } n = 0 \,, \\ 2 & \text{if } n > 0 \,. \end{array} \right.$$

3.1.1. Acoustic domain

Applying the Fourier transform to equation (1) we obtain:

$$\left\{ \begin{array}{rll} d_r^2 \widehat{p}_n + \dfrac{1}{r} d_r \widehat{p}_n + \left(\alpha_f^2 - \dfrac{n^2}{r^2}\right)\widehat{p}_n & = & -\dfrac{A}{2\pi r}\delta(r - r_s) \quad \text{for } 0 \leq r < R \,, \\[3mm] d_r \widehat{p}_n & = & \rho_f \omega^2 \widehat{u}_{r,n} \qquad \qquad \text{at } r = R \,, \end{array} \right. \tag{3}$$

where $\alpha_f = \alpha_f(\xi)$ is the square root, defined by:

$$\alpha_f = \sqrt{k_f^2 - \xi^2} = \left\{ \begin{array}{ll} (k_f^2 - \xi^2)^{1/2} & \text{if } |\xi| \leq k_f \\ -i(\xi^2 - k_f^2)^{1/2} & \text{if } |\xi| > k_f \,. \end{array} \right. \tag{4}$$

Solutions of (3) can be written as a linear combination of Bessel functions $J_n(\alpha_f r)$ and $H_n^{(2)}(\alpha_f r)$. Formally, solving for $\widehat{p}_n$ we obtain:

$$\widehat{p}_n = \frac{J_n(\alpha_f r)}{J_n'(\alpha_f R)} \left(\frac{\rho_f \omega^2}{\alpha_f} \widehat{u}_{r,n}\big|_{r=R} + A\frac{i}{4} J_n(\alpha_f r_s) H_n^{(2)'}(\alpha_f R) \right)$$

$$-A\frac{i}{4} \times \left\{ \begin{array}{ll} J_n(\alpha_f r) H_n^{(2)}(\alpha_f r_s) & \text{if } r < r_s \\ J_n(\alpha_f r_s) H_n^{(2)}(\alpha_f r) & \text{if } r > r_s \,. \end{array} \right. \tag{5}$$

6

Using the Graf's addition theorem (cf. [17]) and the Weyrich's formula (see [18, p.14]), we can verify that the last term in (5), which is defined by parts, corresponds to the Fourier transform of the fundamental solution of the Helmholtz operator in the whole space, i.e.,

$$E = \frac{A}{4\pi} \frac{e^{-ik_f \sqrt{z^2 + r^2 + r_s^2 - 2rr_s \cos\theta}}}{\sqrt{z^2 + r^2 + r_s^2 - 2rr_s \cos\theta}}.$$

Therefore, we only need to take the Fourier inversion for the first term of equation (5), which corresponds to the reflection from the fluid/solid interface, that we denote hereafter by $\widehat{\mathcal{P}}_n$.

3.1.2. Elastic domain

Here we follow an approach similar to [19]. According to equation (2), we represent the field of displacements $\boldsymbol{u} = u_r \boldsymbol{e}_r + u_\theta \boldsymbol{e}_\theta + u_z \boldsymbol{e}_z$ in terms of its scalar and vector potentials, i.e.

$$\boldsymbol{u} = \frac{\nabla \times \boldsymbol{\Psi}}{k_s^2} - \frac{\nabla \Phi}{k_p^2}, \tag{6}$$

where $\Phi = \nabla \cdot \boldsymbol{u}$ and $\boldsymbol{\Psi} = \nabla \times \boldsymbol{u}$. In turn, the vector potential is written in terms of unknown scalar potentials as

$$\boldsymbol{\Psi} = \psi \boldsymbol{e}_z + \frac{1}{k_s^2} \nabla \partial_z \psi + \frac{1}{k_s} \nabla \times (\chi \boldsymbol{e}_z).$$

Taking, respectively, the divergence and the curl of equation (6), we conclude that we need three scalar potentials (namely Φ, ψ, and χ) satisfying the Helmholtz equations:

$$\Delta\Phi + k_p^2 \Phi = 0, \quad \Delta\psi + k_s^2 \psi = 0, \quad \text{and} \quad \Delta\chi + k_s^2 \chi = 0. \tag{7}$$

Explicitly, in the spatial and Fourier (spectral) domains, respectively, we have:

$$u_r = \frac{1}{k_s^2}\left[\frac{1}{k_s}\partial^2_{rz}\chi + \frac{1}{r}\partial_\theta\psi\right] - \frac{1}{k_p^2}\partial_r\Phi, \quad \widehat{u}_{r,n} = -\frac{1}{k_s^2}\left[\frac{i\xi}{k_s}d_r\widehat{\chi}_n + \frac{n}{r}\widehat{\psi}_n\right] - \frac{1}{k_p^2}d_r\widehat{\Phi}_n,$$

$$u_\theta = \frac{1}{k_s^2}\left[\frac{1}{k_s}\frac{1}{r}\partial^2_{\theta z}\chi - \partial_r\psi\right] - \frac{1}{k_p^2}\frac{1}{r}\partial_\theta\Phi, \quad \widehat{u}_{\theta,n} = -\frac{1}{k_s^2}\left[\frac{i\xi}{k_s}\frac{n}{r}\widehat{\chi}_n + d_r\widehat{\psi}_n\right] - \frac{1}{k_p^2}\frac{n}{r}\widehat{\Phi}_n,$$

$$u_z = \frac{1}{k_s^2}\left[k_s\chi + \frac{1}{k_s}\partial^2_z\chi\right] - \frac{1}{k_p^2}\partial_z\Phi, \quad \widehat{u}_{z,n} = \frac{1}{k_s^3}(k_s^2 - \xi^2)\widehat{\chi}_n + \frac{i\xi}{k_p^2}\widehat{\Phi}_n.$$

7

Let α_p and α_s be the square roots defined in the same way as (4), but replacing the wavenumber k_f by the wavenumbers k_p and k_s, respectively. The outgoing solutions of equations (7) in Fourier domain are the Bessel functions $H_n^{(2)}(\alpha_p r)$ and $H_n^{(2)}(\alpha_s r)$. Thus, we can write:

$$\widehat{\Phi}_n = -k_p^2\, c_{1,n}\, H_n^{(2)}(\alpha_p r)\,, \quad \widehat{\psi}_n = -k_s^2\, c_{2,n}\, H_n^{(2)}(\alpha_s r)\,, \text{ and}$$
$$\widehat{\chi}_n = ik_s^3\, c_{3,n}\, H_n^{(2)}(\alpha_s r)\,,$$

for an unknown vector of coefficients $\boldsymbol{c}_n = (c_{1,n}, c_{2,n}, c_{3,n})^T$ that has to be determined using the transmission condition imposed at $r = R$.

In matrix form, we recover the displacements as $\widehat{\boldsymbol{u}}_n = (\widehat{u}_{r,n}, \widehat{u}_{\theta,n}, \widehat{u}_{z,n})^T = \widehat{\boldsymbol{U}}_n \boldsymbol{c}_n$, where $\widehat{\boldsymbol{U}}_n$ has the reduced form:

$$\widehat{\boldsymbol{U}}_n := \begin{pmatrix} \alpha_p H_n^{(2)'}(\alpha_p r) & \dfrac{n}{r} H_n^{(2)}(\alpha_s r) & \xi \alpha_s H_n^{(2)'}(\alpha_s r) \\ \dfrac{n}{r} H_n^{(2)}(\alpha_p r) & \alpha_s H_n^{(2)'}(\alpha_s r) & \xi \dfrac{n}{r} H_n^{(2)}(\alpha_s r) \\ -i\xi H_n^{(2)}(\alpha_p r) & 0 & i\alpha_s^2 H_n^{(2)}(\alpha_s r) \end{pmatrix}.$$

The transmission condition over the fluid/solid interface (see the boundary condition of eq. (2)) is related to the outer pressure $\widehat{p}_n$ of the inner fluid by the formula:

$$\widehat{\boldsymbol{S}}_n \boldsymbol{c}_n = -\widehat{p}_n\big|_{r=R}\, \boldsymbol{e}_r\,, \tag{8}$$

where the coefficients of matrix $\widehat{\boldsymbol{S}}_n$ (related to performing a Fourier transform over the radial stress $\boldsymbol{\sigma}(\boldsymbol{u})\boldsymbol{e}_r$) can be found in Appendix A. Formally, solving for $\widehat{\boldsymbol{u}}_n$, we obtain:

$$\widehat{\boldsymbol{u}}_n = -\widehat{p}_n\big|_{r=R}\, \widehat{\boldsymbol{U}}_n\, \widehat{\boldsymbol{S}}_n^{-1} \boldsymbol{e}_r\,. \tag{9}$$

It will be useful to work with the adjoint matrix of $\widehat{\boldsymbol{S}}_n$ that we define to be $\widehat{\boldsymbol{A}}_n := \det(\widehat{\boldsymbol{S}}_n) \times \widehat{\boldsymbol{S}}_n^{-1}$.

3.1.3. The dispersion relations

To solve equations (5) and (9), we need to calculate the values of $\widehat{p}_n\big|_{r=R}$ and $\widehat{u}_{r,n}\big|_{r=R}$. Thus, evaluating the equations (5) and (9) at $r = R$, and using the Wronskian identity [17], we arrive to the system:

$$\begin{pmatrix} \alpha_f J_n'(\alpha_f R) & -\rho_f \omega^2 J_n(\alpha_f R) \\ \widehat{\boldsymbol{U}}_{1,n} \cdot \widehat{\boldsymbol{A}}_{1,n} & \det(\widehat{\boldsymbol{S}}_n) \end{pmatrix} \begin{pmatrix} \widehat{p}_n \\ \widehat{u}_{r,n} \end{pmatrix}\bigg|_{r=R} = \begin{pmatrix} A\dfrac{J_n(\alpha_f r_s)}{2\pi R} \\ 0 \end{pmatrix}, \tag{10}$$

8

where $\widehat{\boldsymbol{U}}_{1,n}$ stands for the first row vector of matrix $\widehat{\boldsymbol{U}}_n$, while $\widehat{\boldsymbol{A}}_{1,n}$ stands for the first column vector of the adjoint matrix $\widehat{\boldsymbol{A}}_n$.

The determinant of the system in (10) characterizes the dispersion of the guided modes inside the borehole. It has the form:

$$\Delta_n = \alpha_f J_n'(\alpha_f R) \det(\widehat{\boldsymbol{S}}_n) + \rho_f \omega^2 J_n(\alpha_f R) \widehat{\boldsymbol{U}}_{1,n} \cdot \widehat{\boldsymbol{A}}_{1,n} \ .$$

The dispersion relations for guided modes can thus be obtained by looking for the pairs (ξ, ω) such that $\Delta_n(\xi, \omega) = 0$.

Finally, to complete the expression (5) for $\widehat{p}_n$, we compute:

$$\widehat{u}_{r,n}\big|_{r=R} = -A \frac{J_n(\alpha_f r_s)}{2\pi R \, \Delta_n} \, \widehat{\boldsymbol{U}}_{1,n} \cdot \widehat{\boldsymbol{A}}_{1,n} \ .$$

3.2. Singularities

We are interested in computing the inverse Fourier transform of the reflection term $\widehat{\mathcal{P}}_n$. This term contains several real-valued singularities in the ξ-variable which prevents a direct application of numerical inversion techniques like the FFT. The key point in the analysis of these singularities is that, using the Wronskian identity [17], $\widehat{\mathcal{P}}_n$ can be rewritten as:

$$\begin{cases} \widehat{\mathcal{P}}_n = A \dfrac{i}{4} J_n(\alpha_f r) J_n(\alpha_f r_s) \dfrac{\alpha_f H_n^{(2)\prime}(\alpha_f R)\gamma_n + \rho_f \omega^2 H_n^{(2)}(\alpha_f R)\beta_n}{\alpha_f J_n'(\alpha_f R)\gamma_n + \rho_f \omega^2 J_n(\alpha_f R)\beta_n} \ , \\ \text{where} \\ \gamma_n(\omega, \xi^2) = \det(\widehat{\boldsymbol{S}}_n) \quad \text{and} \quad \beta_n(\omega, \xi^2) = \widehat{\boldsymbol{U}}_{1,n} \cdot \widehat{\boldsymbol{A}}_{1,n} \ . \end{cases} \tag{11}$$

Four types of singularities will be analyzed: singularities related to $\alpha_f = 0$, singularities related to $\alpha_p = 0$, singularities related to $\alpha_s = 0$, and singularities related to the determinant $\Delta_n = \alpha_f J_n'(\alpha_f R)\gamma_n + \rho_f \omega^2 J_n(\alpha_f R)\beta_n = 0$.

In the following, we will make use of the following limiting forms for Bessel function and small arguments (cf.[17]), when $z \to 0$:

$$J_n(z) \sim \frac{z^n}{2^n n!} \quad \text{and} \quad iH_n^{(2)}(z) \sim \begin{cases} \dfrac{2}{\pi} \log(z) & \text{if } n = 0 \ , \\ -\dfrac{(n-1)!}{\pi} \dfrac{2^n}{z^n} & \text{if } n > 0 \ , \end{cases} \tag{12}$$

as well as the derivative relation for Bessel functions (cf. [17]) :

$$w \mathcal{B}_n'(w) = n \mathcal{B}_n(w) - w \mathcal{B}_{n+1}(w) \ .$$

9

3.2.1. Singularities related to $\xi^2 = k_f^2$ (or $\alpha_f = 0$).

This singularity is only related with the reflection of the fluid source wave over the boundary $r = R$. It does not contain any information about the formation.

Proposition 1. *All possible singularities related to $\alpha_f = 0$ in $\widehat{\mathcal{P}}_n$ are removable, except when $n = 0$, where there is a log-type singularity.*

Proof. Combining (11) with (12), we obtain for $n \geq 1$:

$$\lim_{\alpha_f \to 0} \widehat{\mathcal{P}}_n = A \frac{r^n r_s^n}{4\pi n R^{2n}} \frac{(n\gamma_n - \rho_f \omega^2 R \beta_n)}{(n\gamma_n + \rho_f \omega^2 R \beta_n)},$$

and for $n = 0$:

$$
\begin{aligned}
\widehat{\mathcal{P}}_0 = & \ A \frac{i}{4} J_0(\alpha_f r) J_0(\alpha_f r_s) \frac{\rho_f \omega^2 \beta_0 H_0^{(2)}(\alpha_f R) - \gamma_0 \alpha_f H_1^{(2)}(\alpha_f R)}{\rho_f \omega^2 \beta_0 J_0(\alpha_f R) - \gamma_0 \alpha_f J_1(\alpha_f R)} \\
\sim & \ A \frac{i}{4} \left[H_0^{(2)}(\alpha_f R) + \mathcal{O}(1) \right],
\end{aligned}
\tag{13}
$$

when $\alpha_f \to 0$. $\qquad\square$

Remark 1. *Singularities associated with the roots of equation $n\gamma_n(\omega, k_f^2) = -\rho_f \omega^2 R \beta_n(\omega, k_f^2)$ exist at the intersection points of the curves defined by $\Delta_n(\xi, \omega) = 0$ and the lines $\xi^2 = k_f^2$. Hence, they are related to the dispersion relation (guide modes).*

3.2.2. Singularities related to $\xi^2 = k_p^2$ (or $\alpha_p = 0$).

This singularity contains the compressional wave information and therefore is related with compressional arrivals at the receivers. We observe a non-smooth behavior of $\widehat{\mathcal{P}}_n$ at these points, given by the change of sign inside the square root α_p. The non-smoothness is more pronounced for $n = 0$.

Proposition 2. *All possible singularities related to $\alpha_p = 0$ in $\widehat{\mathcal{P}}_n$ are removable, except when $n = 0$, where a singularity associated with the Bessel function $H_0^{(2)}(\alpha_p R)$ may arise for particular frequencies.*

Proof. Observe, that γ_n and β_n can be factorized as:

$$
\left\{
\begin{aligned}
\gamma_n = & \ \widehat{\boldsymbol{S}}_{11,n} \widehat{\boldsymbol{A}}_{11,n} + \widehat{\boldsymbol{S}}_{21,n} \widehat{\boldsymbol{A}}_{12,n} + \widehat{\boldsymbol{S}}_{31,n} \widehat{\boldsymbol{A}}_{13,n} \,, \\
\beta_n = & \ \widehat{\boldsymbol{U}}_{11,n} \widehat{\boldsymbol{A}}_{11,n} + \widehat{\boldsymbol{S}}_{21,n} \beta_{21,n} + \widehat{\boldsymbol{S}}_{31,n} \beta_{31,n} \,,
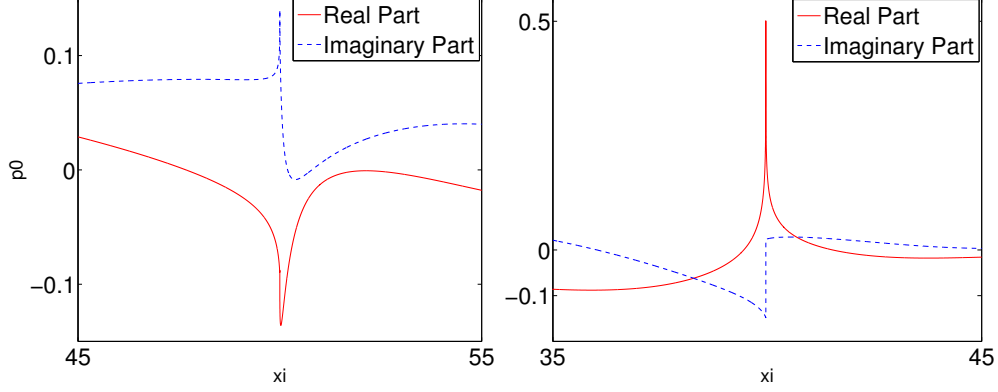\end{aligned}
\right.
\tag{14}
$$

10

Figure 2: Typical behavior of $\widehat{\mathcal{P}}_0$ in a neighborhood of $\xi = k_p$. Left panel: the case when we are far from a resonant frequency. Right panel: resonant frequency case.

where

$$\beta_{21,n} = \widehat{\boldsymbol{U}}_{13,n}\widehat{\boldsymbol{S}}_{32,n} - \widehat{\boldsymbol{U}}_{12,n}\widehat{\boldsymbol{S}}_{33,n} \quad \text{and} \quad \beta_{31,n} = \widehat{\boldsymbol{U}}_{12,n}\widehat{\boldsymbol{S}}_{23,n} - \widehat{\boldsymbol{U}}_{13,n}\widehat{\boldsymbol{S}}_{22,n}\,.$$

The only singular terms (when $\alpha_p = 0$) are $\widehat{\boldsymbol{U}}_{11,n}$ and $\widehat{\boldsymbol{S}}_{j1,n}$, for $j = 1, 2, 3$. Using the limit forms (12), we obtain as $\alpha_p \to 0$ for $n \geq 1$:

$$\widehat{\boldsymbol{U}}_{11,n} = \mathcal{O}(\alpha_p^{-n}) \quad \text{and} \quad \widehat{\boldsymbol{S}}_{j1,n} = \mathcal{O}(\alpha_p^{-n})\,, \quad \text{for } j = 1, 2, 3\,.$$

Hence, for $n \geq 1$, the terms in the numerator of $\widehat{\mathcal{P}}_n$ are of the same order as the terms in the denominator. Thus, $\widehat{\mathcal{P}}_n$ has a finite limit as $\alpha_p \to 0$. However, for $n = 0$ and $\alpha_p \to 0$ we obtain:

$$\widehat{\boldsymbol{U}}_{11,n} = \mathcal{O}(1)\,, \quad \widehat{\boldsymbol{S}}_{11,n} \sim H_0^{(2)}(\alpha_p R)\,, \quad \widehat{\boldsymbol{S}}_{21,n} = 0\,, \quad \text{and} \quad \widehat{\boldsymbol{S}}_{31,n} = \mathcal{O}(1)\,.$$

Therefore, $\gamma_0 \sim H_0^{(2)}(\alpha_p R) + \mathcal{O}(1)$ in this case, while $\beta_0 = \mathcal{O}(1)$. The terms in the numerator of $\widehat{\mathcal{P}}_0$ will be of the same order as the terms in the denominator, except for frequencies such that $J_1(\sqrt{k_f^2 - k_p^2}R) = 0$. If this last situation occurs, then the denominator of $\widehat{\mathcal{P}}_0$ will have a different order than the numerator, and a log-type singularity related to $H_0^{(2)}(\alpha_p R)$ will appear. $\qquad\square$

Remark 2. *In general, the asymptotic expression for γ_0 affects the smoothness of $\widehat{\mathcal{P}}_0$ when $\alpha_p = 0$. We observe a log-type singularity if we match with a frequency for which $J_1(\sqrt{k_f^2 - k_p^2}R) = 0$ (see Fig. 3). In any case, the function $\widehat{\mathcal{P}}_0$ is integrable in a neighborhood of $\xi = \pm k_p$.*

11

3.2.3. Singularities related to $\xi^2 = k_s^2$ (or $\alpha_s = 0$).

This singularity contains the shear wave information and therefore is related with shear arrivals at the receivers. We observe a non-smooth behavior of $\widehat{\mathcal{P}}_n$ at these points, given by the change of sign inside the square root α_s. The non-smoothness is more pronounced for $n = 1$.

Proposition 3. *All possible singularities related to $\alpha_s = 0$ in $\widehat{\mathcal{P}}_n$ are removable, except those located at the intersection points of the dispersion curves $\Delta_n = 0$ with the lines $\xi^2 = k_s^2$.*

Proof. Again, we make use of expression (14) for γ_n and β_n, and the limit forms (12). Provided that $\alpha_s = 0$, the singular terms in (14) are $\widehat{\boldsymbol{A}}_{1j,n}$ (for $j = 1, 2, 3$) and $\beta_{j1,n}$ (for $j = 2, 3$). When $n = 0$, we only need to analyze $\widehat{\boldsymbol{A}}_{11,n} = \widehat{\boldsymbol{S}}_{22,n}\widehat{\boldsymbol{S}}_{33,n}$, $\widehat{\boldsymbol{A}}_{13,n} = -\widehat{\boldsymbol{S}}_{22,n}\widehat{\boldsymbol{S}}_{13,n}$, and $\beta_{31,n} = -\widehat{\boldsymbol{U}}_{13,n}\widehat{\boldsymbol{S}}_{22,n}$ (the remaining terms are multiplied by zero). We obtain:

$$\widehat{\boldsymbol{A}}_{11,0} = \mathcal{O}(1)\,, \quad \widehat{\boldsymbol{A}}_{13,0} = \mathcal{O}(1)\,, \quad \text{and} \quad \beta_{31,0} = \mathcal{O}(1)\,, \quad \text{as } \alpha_s \to 0\,.$$

For the case $n = 1$, we have:

$$\widehat{\boldsymbol{A}}_{11,1} \sim H_0^{(2)}(\alpha_s R) + \mathcal{O}(1)\,, \quad \widehat{\boldsymbol{A}}_{12,1} \sim H_0^{(2)}(\alpha_s R) + \mathcal{O}(1)\,, \quad \widehat{\boldsymbol{A}}_{13,1} = \mathcal{O}(1)\,,$$

$$\beta_{21,1} = \mathcal{O}(1)\,, \quad \text{and} \quad \beta_{31,1} \sim H_0^{(2)}(\alpha_s R) + \mathcal{O}(1)\,, \quad \text{as } \alpha_s \to 0\,.$$

For $n \geq 2$, all the terms behave like $\mathcal{O}(\alpha_s^{2(1-n)})$. Hence, for every $n \geq 0$, we observe that γ_n is of the same order as β_n. Thus, the terms in the numerator of $\widehat{\mathcal{P}}_n$ are of the same order as the terms in the denominator and the existing singularities cancel out. Other singularities related to $\Delta_n = 0$ (guided modes) will be discussed in what follows. $\qquad\square$

Remark 3. *The asymptotic expressions for γ_1 and β_1 in terms of Bessel functions $H_0(\alpha_s R)$ affect the smoothness of $\widehat{\mathcal{P}}_1$ when $\alpha_s = 0$. Nevertheless, the function is still finite and integrable (similar to Fig. 3, left panel).*

3.2.4. Singularities related to $\Delta_n = 0$.

Finally, we comment on the singularities related to the roots of $\Delta_n = 0$. These singularities contain all the information about the guided modes inside the cylinder. The ones that can be detected at the receivers are typically those related with low values of n. For a fixed frequency, we use a root finder routine to compute the roots assuming *a priori* information available in literature (cf. [20] or [21]). We assume the following:

- Every root of Δ_n is a simple root. If ξ_j is a root, also it is $-\xi_j$. So the singularity of $\widehat{\mathcal{P}_n}$ related to the roots $\pm\xi_j$ behaves like $\mathcal{O}(\frac{1}{\xi^2 - \xi_j^2})$.

- For $n = 0$, there is at least one root associated with the Stoneley mode which (in most applications) exists for each frequency $\omega > 0$. The low-frequency limit of the Stoneley mode is given by [21]:

$$\xi_{\mathrm{ST}} = \frac{\omega}{c_{\mathrm{ST}}}, \quad \text{where} \quad c_{\mathrm{ST}} = \frac{c_f}{\sqrt{1 + \rho_f c_f^2/\mu}} < c_f .$$

In a slow formation $(k_p < k_f < k_s)$:

- For each $n \geq 0$ and fixed $\omega > 0$, there is at most one root of Δ_n. The root approaches asymptotically the wavenumber of the Scholte wave [21] (which is larger than k_s) in a high-frequency limit.

- For $n \geq 1$, the root appears for every frequency larger than a characteristic cut-off frequency. At the cut-off frequency this root matches with the shear wavenumber k_s.

In a fast formation $(k_p < k_s < k_f)$:

- For each $n \geq 0$ and fixed $\omega > 0$, there is a finite number of roots of Δ_n. The roots have their respective cut-off frequencies ($\omega = 0$ for the Stoneley mode). At the cut-off frequencies, the roots match with the shear wavenumber k_s.

- For each $n \geq 0$, the root with the lowest cut-off frequency approaches to the wavenumber of the Scholte wave as ω grows. The remaining roots approach k_f in the high-frequency limit.

3.3. Inverse Transform

In this subsection we describe how to recover the spatial solution by means of the inverse Fourier transform. First, we analyze the case of a point source. To recover the spatial solution, we perform:

$$p = E + \frac{1}{2\pi} \int_{\mathbb{R}} \widehat{\mathcal{P}}_0(\xi) e^{-i\xi z} d\xi + \frac{1}{\pi} \sum_{n \geq 1} \cos n\theta \int_{\mathbb{R}} \widehat{\mathcal{P}}_n(\xi) e^{-i\xi z} d\xi . \qquad (15)$$
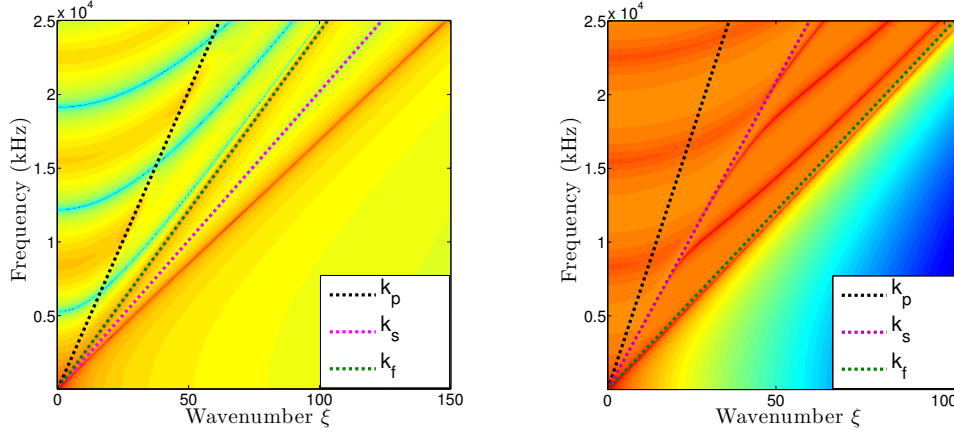
13

Figure 3: Log of the modulus of $\widehat{\mathcal{P}}_0$ as a function of ξ and frequency $f = \frac{\omega}{2\pi}$. Left panel: slow formation case. The red curve is the singularity associated with the Stoneley mode, while blue curves are zeros of Bessel function $J_0(\alpha_f R)$. Right panel: fast formation case. We observe four curves of singularities (in red). The one under the fluid wavenumber line is the Stoneley mode, while the other three have cut-off frequencies at shear wavenumber.

As discussed in the previous section, the reflection terms $\widehat{\mathcal{P}}_n$ ($n \geq 0$) have singularities that prohibit a direct evaluation of the integrals in (15). The idea is to split each $\widehat{\mathcal{P}}_n$ into a sum of a singular (non-integrable) and a regular (integrable) part:

$$\widehat{\mathcal{P}}_n = \widehat{\mathcal{P}}_n^{\text{sing}} + \widehat{\mathcal{P}}_n^{\text{reg}} . \tag{16}$$

It is important to characterize properly the singular part. The regular part is then obtained by using (16). The inverse Fourier transform of the singular part is treated analytically in a distributional sense, while the regular part is treated numerically with the FFT technique, i.e.,

$$\int_{\mathbb{R}} \widehat{\mathcal{P}}_n^{\text{reg}} e^{-i\xi z} d\xi = \int_{\mathbb{R}} (\widehat{\mathcal{P}}_n - \widehat{\mathcal{P}}_n^{\text{sing}}) e^{-i\xi z} d\xi \approx \text{FFT}[\widehat{\mathcal{P}}_n - \widehat{\mathcal{P}}_n^{\text{sing}}] .$$

3.3.1. Treatment of the singular part

For each $\omega > 0$ and $n \in \mathbb{N}$, we define Nsing $=$ Nsing(ω, n) to be the number (possible zero) of singularities related to the roots of $\Delta_n = 0$. For each singularity $\xi_j = \xi_j(\omega, n) > 0$ ($j = 1, ..., \text{Nsing}(\omega, n)$) we compute the residue:

$$\text{Res}_j(\omega, n) = \lim_{\xi^2 \to \xi_j^2} (\xi^2 - \xi_j^2) \widehat{\mathcal{P}}_n .$$

14

Thus, recalling that $\widehat{\mathcal{P}}_0$ has an extra singularity as $\alpha_f \to 0$ (see subsection 3.2.1), we define the singular contribution as:

$$
\widehat{\mathcal{P}}_n^{\text{sing}} = \begin{cases} A\dfrac{i}{4}H_0^{(2)}(\alpha_f R) + \displaystyle\sum_{j=1}^{\text{Nsing}} \dfrac{\text{Res}_j}{(\xi^2 - \xi_j^2)}, & \text{if } n = 0\,, \\[2em] \displaystyle\sum_{j=1}^{\text{Nsing}} \dfrac{\text{Res}_j}{(\xi^2 - \xi_j^2)}, & \text{if } n \geq 1\,. \end{cases}
$$

Now, using the inversion formulas provided by [18, 22], we obtain:

$$
\int_{\mathbb{R}} \widehat{\mathcal{P}}_n^{\text{sing}} e^{-i\xi z} d\xi = \begin{cases} -\dfrac{A}{2}\dfrac{e^{-ik_f\sqrt{R^2+z^2}}}{\sqrt{R^2+z^2}} - i\pi \displaystyle\sum_{j=1}^{\text{Nsing}} \dfrac{\text{Res}_j}{\xi_j} e^{-i\xi_j|z|} & \text{if } n = 0\,, \\[2em] -i\pi \displaystyle\sum_{j=1}^{\text{Nsing}} \dfrac{\text{Res}_j}{\xi_j} e^{-i\xi_j|z|} & \text{if } n \geq 1\,. \end{cases}
$$

3.4. The multipole source eccentered model

We consider infinitesimal point sources placed along an eccentered circle of radius r_a :

$$
S := \big\{(r_c, 0) + (r_a \cos\theta_a, r_a \sin\theta_a) : 0 \leq \theta_a < 2\pi\big\},
$$

where r_c (the eccentricity) and r_a are such that $r_c + r_a < R$ (the radius of the borehole). Each single point source has a characteristic amplitude $A = \cos(m(\theta_a - \varphi))$, where $m \geq 0$. This model can describe: monopole ($m = 0$), dipole ($m = 1$), quadrupole ($m = 2$), as well as higher order sources. The angle $\varphi \in [0, 2\pi)$ can be used to rotate the axis of the sources. Using this setting, the excitation term can be expressed as:

$$
\mathcal{E} = \frac{r_a}{4\pi} \int_0^{2\pi} \frac{e^{-ik_f\sqrt{(x-x_s)^2+(y-y_s)^2+z^2}}}{\sqrt{(x-x_s)^2 + (y-y_s)^2 + z^2}}\, \cos(m(\theta_a - \varphi))\, d\theta_a\,,
$$

where $(x, y) = (r\cos\theta, r\sin\theta)$ and $(x_s, y_s) = (r_c + r_a \cos\theta_a, r_a \sin\theta_a)$. The spatial response in (r, θ, z) can be expressed formally as:

$$
\mathcal{P} = \mathcal{E} + \frac{r_a}{\pi} \int_{\mathbb{R}} \left(\int_0^{2\pi} \frac{\widehat{\mathcal{P}}_0(\xi)}{2} + \sum_{n\geq 1} \cos(n(\theta - \theta_s))\widehat{\mathcal{P}}_n(\xi)\, d\theta_a \right) e^{-i\xi z} d\xi\,,
$$

15

where (r_s, θ_s) are the polar coordinates of (x_s, y_s), and for $n \geq 0$,

$$\widehat{\mathcal{P}}_n = \frac{i}{4} J_n(\alpha_f r) J_n(\alpha_f r_s) \frac{\gamma_n \alpha_f R H_n^{(2)'}(\alpha_f R) + \beta_n H_n^{(2)}(\alpha_f R)}{\gamma_n \alpha_f R J_n'(\alpha_f R) + \beta_n J_n(\alpha_f R)} \cos(m(\theta_a - \varphi)).$$

Notice that the singularities remain invariant to the source positions, since they solely depend on the geometry of the problem and the material properties. The same decomposition technique into singular and regular parts apply for this case.
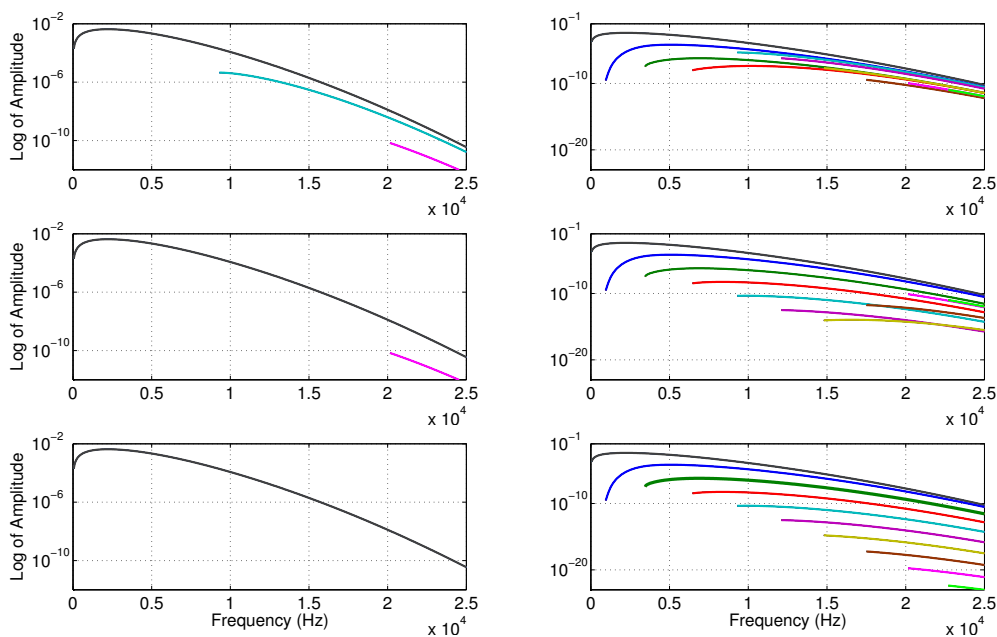
Figure 4: Log of the amplitudes of the excited propagative modes from $n = 0$ to $n = 9$ in a slow formation monopole setting. First column: centered case using 4, 8 and 16 source points respectively. Second column: same as first column, but considering one centimeter of eccentricity.

In practice, the angular integral in the θ_a-variable is calculated using the trapezoidal rule. This is perhaps a more realistic model, since actual logging devices work with four or eight sources uniformly distributed over the ring. However, we remark that additional modes may appear by using this technique, and they are physically correct. The latter may be avoided by considering finite-size sources along the azimuthal direction, or by increasing the number of point sources over the ring. The reason is simple: for example,

16

let us consider the centered case ($r_c = 0$) and M points uniformly distributed over the ring, i.e., $\{r_a e^{i\theta_s} : \theta_s = 2\pi s/M, s = 1, ..., M\}$. For the monopole case ($m = 0$) the reflection term reduces to:

$$\mathcal{P} - \mathcal{E} = r_a \int_{\mathbb{R}} \left(\widehat{\mathcal{P}}_0(\xi) + \frac{2}{M} \sum_{s=1}^{M} \sum_{n \geq 1} \cos(n(\theta - \theta_s))\widehat{\mathcal{P}}_n(\xi) \right) e^{-i\xi z} d\xi .$$

The sum $\sum_{s=1}^{M} \cos(n(\theta - \theta_s))$ vanishes unless n is a multiple of M. The larger the M, the smaller the contribution of $n = M, 2M, ...$ in the sum. For $M = 8$, the contribution of $n = 8$ is probably negligible, while for $M = 4$ (the case considered in [15]) the contribution of $n = 4$ may not be negligible and could confuse the interpretation of post-processed data (see Fig. 4).

4. Numerical results

4.1. Verification with other methods.

In this section, we verify our method by comparing our results against those obtained by other numerical techniques.
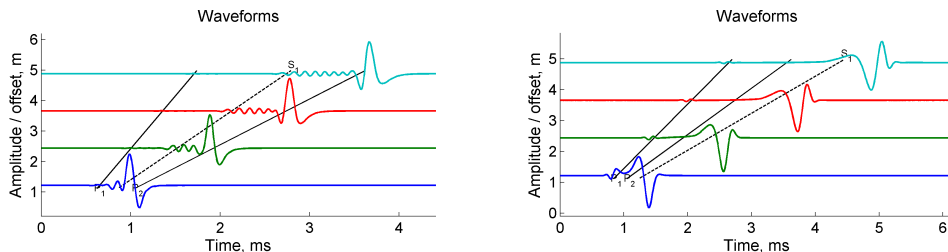
Figure 5: Full waveforms excited by a 5 kHz source. Left panel: fast formation. Right panel: slow formation.

We start comparing with the method used by Kurkjian [6], in which the Fourier integration along the real axis is replaced by integration along the paths on each side of the branch cuts of the square roots α_p and α_s, plus residual contributions of the singularities given by the roots of $\Delta_n = 0$. The parameters for a fast and slow formation are given in [6, Table 1]. We reproduce waveforms excited by a pulse, the second derivative of a Blackman-Harris window function (cf. [23]), with a 5 kHz central frequency. This means that we had computed responses for several frequencies, and used an extra FFT to recover the time domain solution. In Fig. 5, we display the waveforms
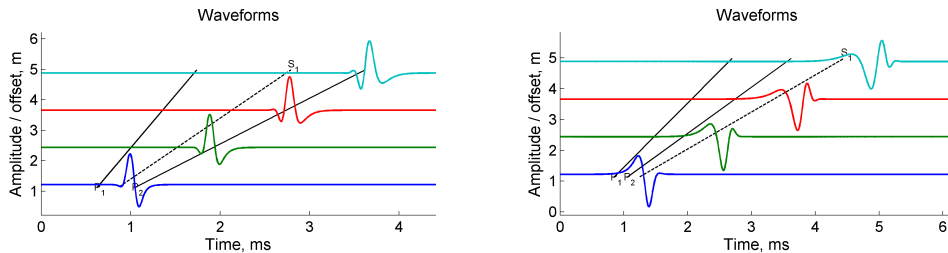
Figure 6: Tube (Stoneley) mode. Left panel: fast formation. Right panel: slow formation.
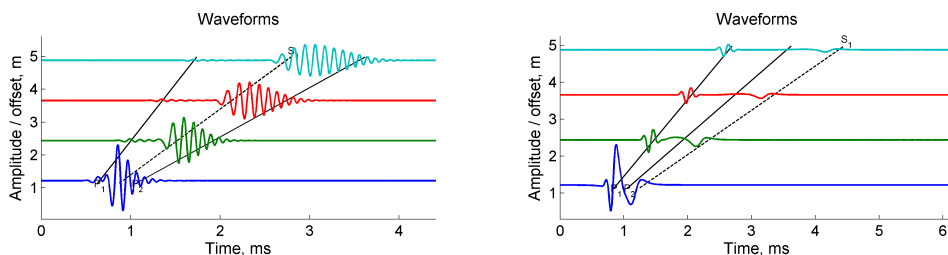

Figure 7: Full waveform minus tube mode. Left panel: fast formation. Right panel: slow formation.

analogously to those in [6, Fig. 10a & Fig. 5]. In Fig. 6, we show the tube mode waveform analogously to that in [6, Fig. 10b & Fig. 6c]. In Fig. 7, we display the full waveforms minus the tube mode analogously to the one described in [6, Fig. 12a & Fig. 8a]. In each case, we observe that results are identical (up to a scaling factor on the amplitudes), without using any complex integration path.

Next, we compare results obtained with our method versus those obtained with a high-order adaptive finite-element method [1]. In this case, we have used a 5 kHz ring source in a slow formation for several borehole-eccentered distances r_c. We display the normalized pressure at a monopole (ring) receiver as a function of the distance from the ring source (transmitter). Results match very accurately, as it can be observed in Fig. 8.

4.2. Numerical experiment: Convergence of the FFT.

The proposed method builds upon the idea of separating singularities from the regular part of the integrand when performing the inverse Fourier transform. We expect then a nice convergence of the FFT treatment of that regular part. This is exactly what we observe in the following experiment. We fix an upper integration limit for the FFT and then consider an increasing
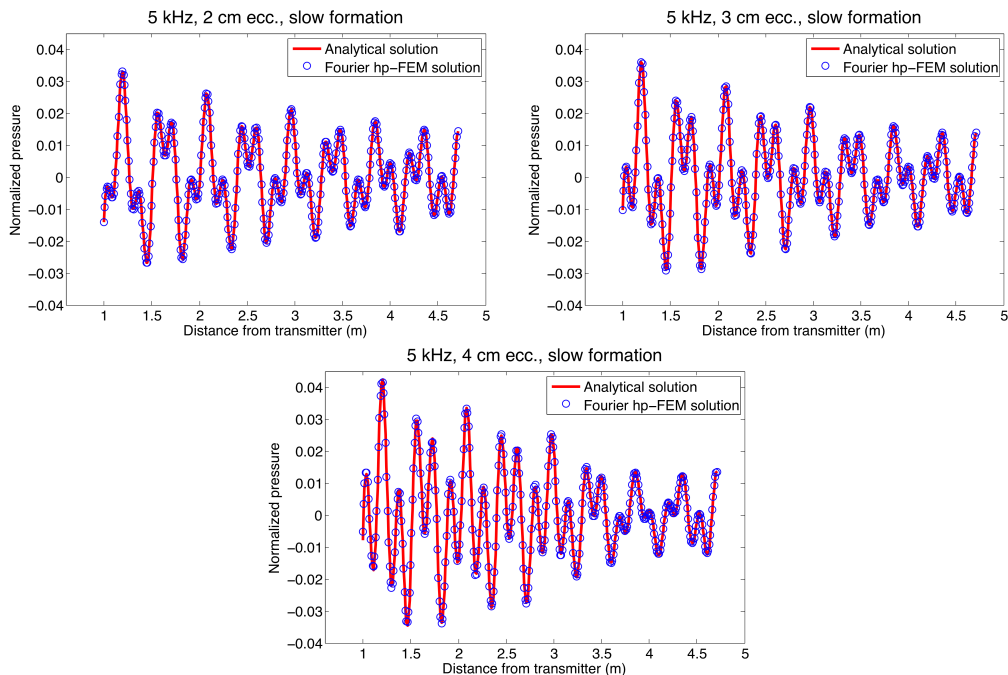
Figure 8: Comparison of the numerical solution to the analytical one for a borehole-eccentered sonic logging problem at 5 kHz. Different panels correspond to various distances between the center of sources/receivers and the axis of symmetry.

sequence of meshes from 2^{10} nodes up to 2^{20} nodes. In each of the meshes we compute the same problem, a 10KHz centered monopole in fast formation which originally has three singularities. Additionally, to also test the convergence of the RAI method, we add an imaginary part $\omega_I > 0$ to the angular frequency and perform a direct FFT without extracting the singularities (recall that singularities are shifted to the complex plane in this case). In Fig. 9, we display the relative error between the results of two consecutive meshes. The solid line is the convergence history obtained by our proposed technique, which is very stable. The dashed lines correspond to the FFT convergence of the RAI method with increasing imaginary parts $\omega_I > 0$. We observe that ω_I has to be rather large in order to obtain reasonable results.

4.3. Numerical experiment: Approaching the borehole wall.

In this experiment, we show how increasing the eccentricity in such a way that the source approaches the borehole wall, increases the amplitudes of higher order modes.

19
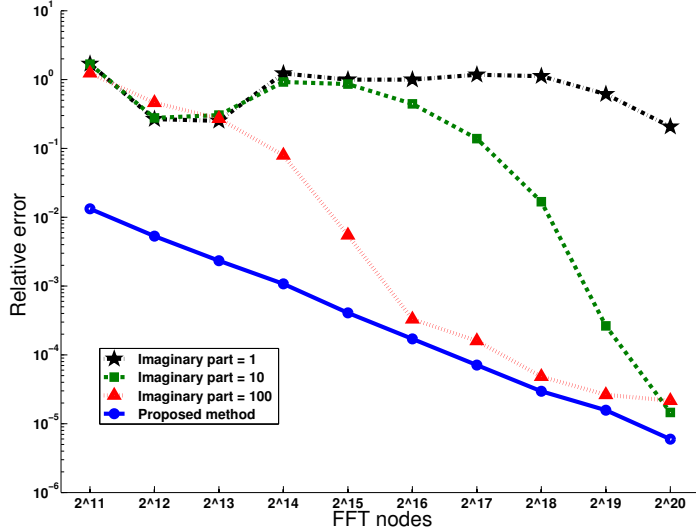
Figure 9: FFT convergence for our proposed method and for the RAI method with different imaginary parts.

In the eccentric model, higher order guided modes always exist. However, they are to small to be detected by a post-processing algorithm. One can always compute the dispersion curve of such modes with a root-finding technique (see Fig. 10), but we do not know if the modes have an important contribution to the solution or not. The last can only be observed by computing the amplitude of each mode independently. As we approach the borehole wall, the amplitudes of higher order modes grow and they converge to the limiting scenario in which the source is located at the borehole wall.

	ρ (kg/m^3)	$\mathbf{V_P}$ (m/s)	$\mathbf{V_s}$ (m/s)	Borehole radius (m)	0.1097
Formation	2100	2540	1269	Imaginary tool radius (m)	0.045
Fluid	1100	1524	–	Number of source points	16

Table 1: Assumed material properties and geometry of the problem.

The material properties and geometry of this experiment are given in Table 1. We used an eccentered monopole source in slow formation assuming equal strength of the source for every frequency. Thus, we display the so-called *raw spectra* (see Fig. 11). We only plot amplitudes over a 10^{-5}
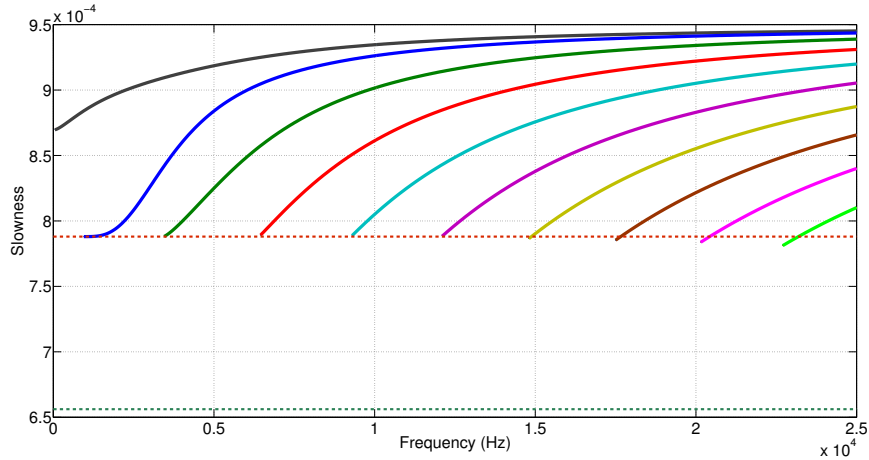
Figure 10: Slowness curves of the first ten cylindrical modes in the slow formation setting of Table 1. Every other mode appears after 25 KHz.

threshold. When the ring source is at 3cm from the borehole wall, only four cylindrical modes exist (Fig. 11, top left). Incrementing the eccentricity in 1cm generates an increase of the amplitudes of every mode (Fig. 11, top right). When further rising the eccentricity by 1 more cm., we observe seven modes over the 10^{-5} threshold (Fig. 11, bottom left). Finally, when the source is at the borehole wall, every cylindrical mode (whose cut-off frequency is under 25 KHz) is over the 10^{-5} threshold (Fig. 11, bottom right).

4.4. Numerical experiment: eccentered/rotated dipole and quadrupole sources

We conclude this section showing a physically interesting phenomena. When using a centered dipole ($n = 1$) or a quadrupole ($n = 2$) source there is no Stoneley mode contribution. In the eccentered case, however, the situation changes. As we increase the eccentricity, modes of all orders (including lower and higher-order modes) are excited. Particularly, eccentered dipole or quadrupole sources can excite the Stoneley mode. However, it is possible to eliminate the Stoneley mode contribution by rotating the source by 90° for the dipole, and by 45° in the quadrupole case. The latter is independent of the amount of eccentricity used.

The material properties and geometry of this experiment are given in Table 1. We work with slow formation and two borehole-eccentered distances. The first one is 2.5 cm, and the second one is 5.0 cm (just 1.47 cm
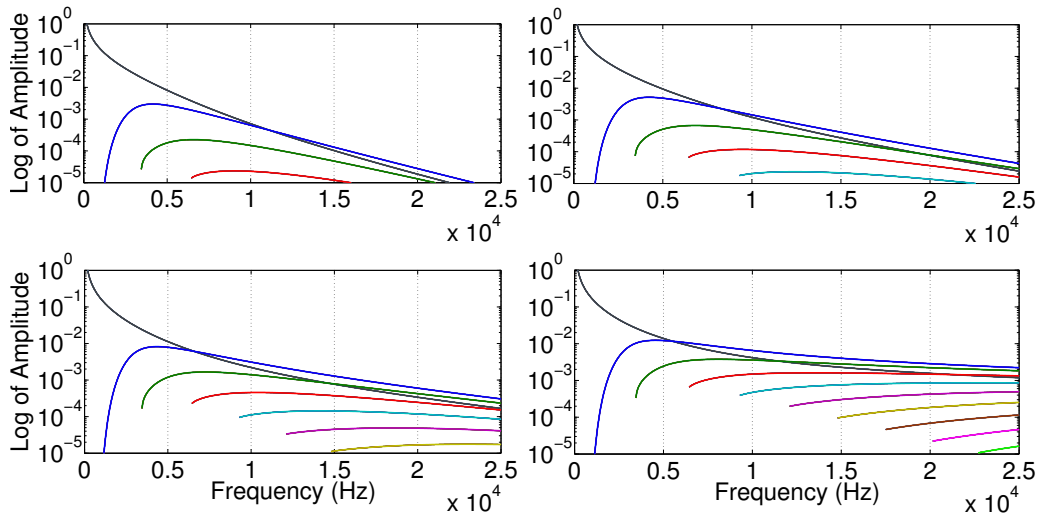
21

Figure 11: Amplitudes of the excited cylindrical modes due to an eccentered monopole source. From left to right and from top to bottom, the distances of the ring source to the borehole wall are 3cm, 2cm, 1cm and 0cm respectively.

from the borehole wall). We compute the amplitudes of the excited borehole modes. In the dipole case (Fig. 12), we have used the Ricker wavelet source at central frequency at 5 kHz. Results for four different rotation angles $\left\{ \varphi = \frac{\pi}{2}(\frac{l-1}{l}) : l = 1, 10, 100, 1000 \right\}$ are presented. Hence, for $l = 1$, there is no rotation and for $l = 1000$, we approach $90°$. The left column shows the results for $r_c = 2.5$ cm. We observe that only the first five modes $(n = 0, 1, 2, 3, 4)$ contribute with amplitudes above the 10^{-8} threshold. The amplitude of the Stoneley mode (black line) vanishes as we approach the $90°$ rotation, while the amplitudes of other modes remain almost invariant. Analogously, the right column shows the results for $r_c = 5.0$ cm. As we approach the borehole wall, the contributions of higher-order modes are larger. We observe amplitudes above the 10^{-8} threshold for the first seven modes $(n = 0, 1, 2, 3, 4, 5, 6)$. The amplitude of the Stoneley mode also vanishes as we approach the $90°$ rotation.

The quadrupole case (Fig. 13) is very similar. We have used the Ricker wavelet at central frequency 6 kHz, and we display results for four rotation angles $\left\{ \varphi = \frac{\pi}{4}(\frac{l-1}{l}) : l = 1, 10, 100, 1000 \right\}$, where mode amplitudes are above 10^{-11}. The left column shows the case $r_c = 2.5$ cm and it involves contributions from the first eight modes $(n = 0, ..., 7)$. The right column shows the case $r_c = 5$ cm and it involves contributions from the first ten modes
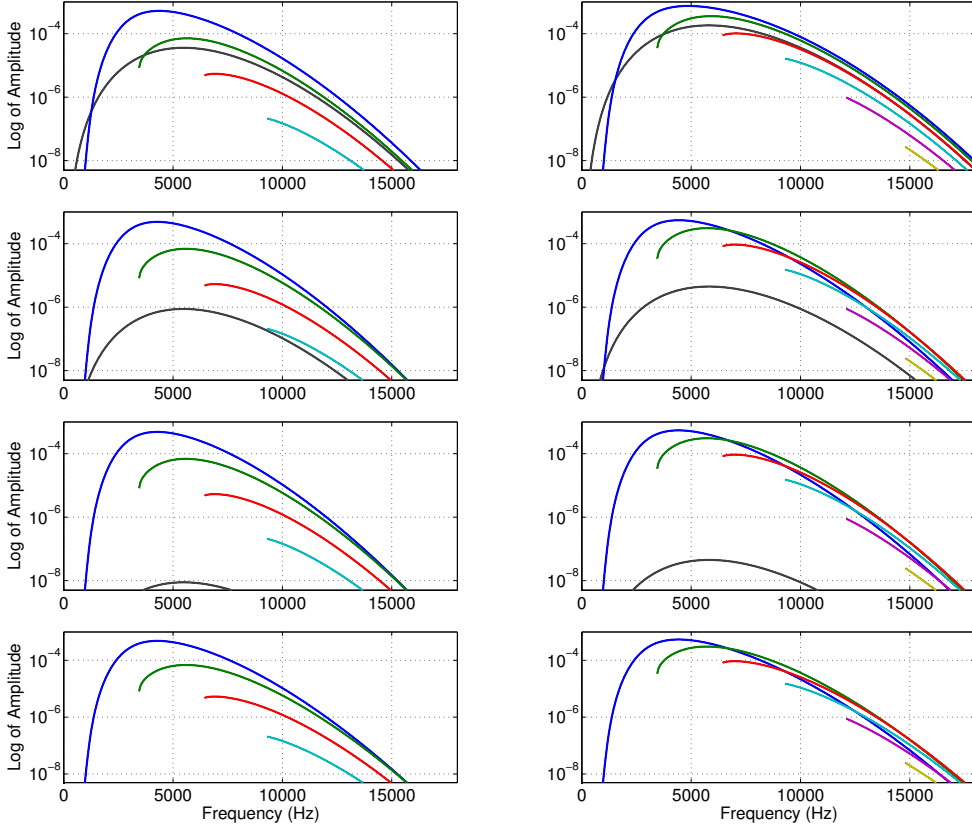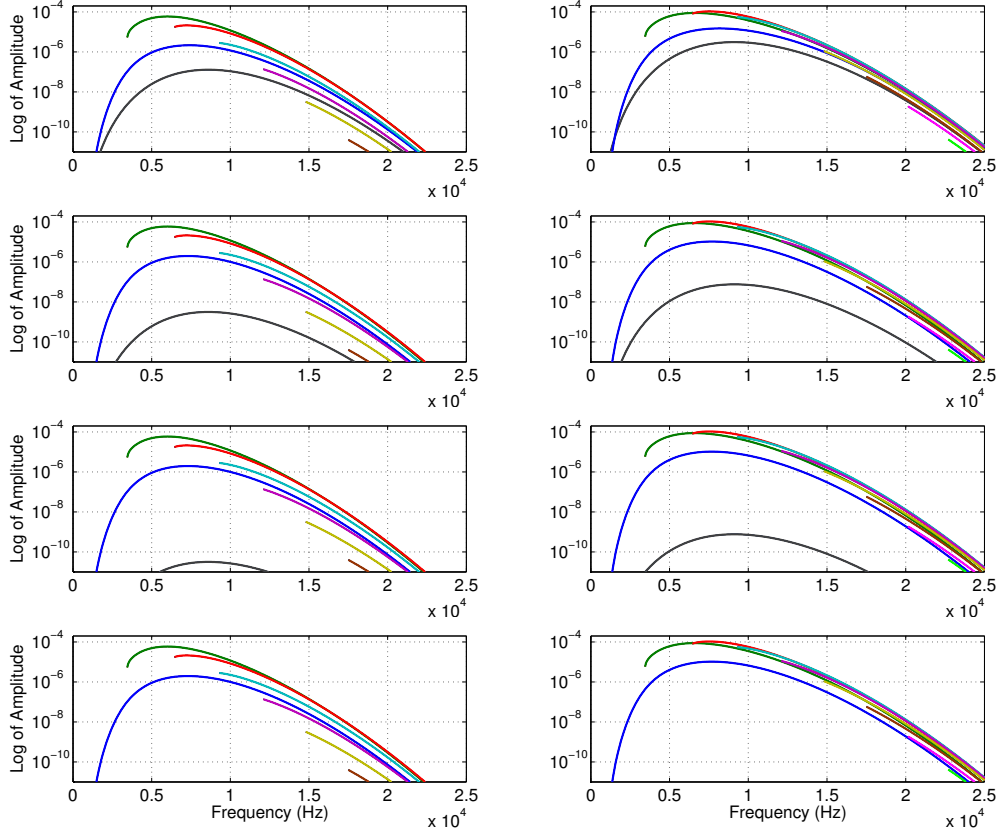
Figure 12: Amplitudes of the excited modes for an eccentered/rotated dipole source. Left column: 2.5 cm of eccentricity. Right column: 5.0 cm of eccentricity. From top to bottom: rotation by 0, $\frac{9}{20}\pi$, $\frac{99}{200}\pi$ and $\frac{999}{2000}\pi$ degrees respectively.

$(n = 0, ..., 9)$. In both situations, we observe that the amplitude of the Stoneley mode vanishes as we approach the $45°$ rotation, while the amplitudes of other modes remain almost invariant.

Further 3D numerical experiments for the case of borehole-eccentered measurements with dipole excitation [24] confirm that similar effects are also observed in the presence of a mandrel, where a rotation of the tool may significantly reduce the amplitude of the compressional wave.

5. Conclusions

We have described a semi-analytical method for simulation of acoustic logging measurements due to (time-harmonic) multipole eccentered sources.

Figure 13: Amplitudes of the excited modes for an eccentered/rotated quadrupole source. Left column: 2.5 cm of eccentricity. Right column: 5.0 cm of eccentricity. From top to bottom: rotation by 0, $\frac{9}{40}\pi$, $\frac{99}{400}\pi$ and $\frac{999}{4000}\pi$ degrees respectively.

The method consists of separating singularities from the smooth part of the solution within the Fourier domain, and then, treating both components of the solution separately when performing the inverse Fourier transform. The resulting procedure is simple to implement and provides very effective simulations and understanding of borehole-eccentered sonic measurements phenomena. The method is built on separating the modal contributions from the full solution, so the acquisition of dispersion curves is fast and straightforward (time-domain methods need post-processing algorithms to recover this data). The last property provides a powerful tool to help the interpretation of borehole-eccentered measurements in real-time. Numerical experiments indicate that we matched the results obtained by other methods existing in

24

the literature. Moreover, we are able to accurately simulate situations in which the sources and transmitters are arbitrarily close to the borehole wall.

Acknowledgment

Appendix A. The stress matrix $\widehat{\boldsymbol{S}}_n$

Matrix $\widehat{\boldsymbol{S}}_n$ gives the Fourier transform of the radial stress $\boldsymbol{\sigma}(\boldsymbol{u})\boldsymbol{e}_r$ at the boundary $r = R$ (see eq. (8)). The coefficients of $\widehat{\boldsymbol{S}}_n$ are:

$$
\begin{aligned}
\widehat{\boldsymbol{S}}_{11,n} &= \mu\left(2\tfrac{n^2}{R^2} - (\alpha_s^2 - \xi^2)\right)H_n^{(2)}(\alpha_p R) - 2\mu\tfrac{\alpha_p}{R}H_n^{(2)'}(\alpha_p R) \\
\widehat{\boldsymbol{S}}_{12,n} &= 2\mu n\left(\tfrac{\alpha_s}{R}H_n^{(2)'}(\alpha_s R) - \tfrac{1}{R^2}H_n^{(2)}(\alpha_s R)\right) \\
\widehat{\boldsymbol{S}}_{13,n} &= -2\mu\xi\left(\tfrac{\alpha_s}{R}H_n^{(2)'}(\alpha_s R) + (\alpha_s^2 - \tfrac{n^2}{R^2})H_n^{(2)}(\alpha_s R)\right) \\
\widehat{\boldsymbol{S}}_{21,n} &= 2\mu n\left(\tfrac{1}{R^2}H_n^{(2)}(\alpha_p R) - \tfrac{\alpha_p}{R}H_n^{(2)'}(\alpha_p R)\right) \\
\widehat{\boldsymbol{S}}_{22,n} &= \mu(\alpha_s^2 - 2\tfrac{n^2}{R^2})H_n^{(2)}(\alpha_s R) + 2\mu\tfrac{\alpha_s}{R}H_n^{(2)'}(\alpha_s R) \\
\widehat{\boldsymbol{S}}_{23,n} &= 2\mu\xi n\left(\tfrac{1}{R^2}H_n^{(2)}(\alpha_s R) - \tfrac{\alpha_s}{R}H_n^{(2)'}(\alpha_s R)\right) \\
\widehat{\boldsymbol{S}}_{31,n} &= i2\mu\xi\tfrac{\alpha_p}{R}H_n^{(2)'}(\alpha_p R) \\
\widehat{\boldsymbol{S}}_{32,n} &= i\mu\xi n\tfrac{1}{R^2}H_n^{(2)}(\alpha_s R) \\
\widehat{\boldsymbol{S}}_{33,n} &= i\mu(\xi^2 - \alpha_s^2)\tfrac{\alpha_s}{R}H_n^{(2)'}(\alpha_s R)
\end{aligned}
$$

[1] D. Pardo, P. Matuszyk, I. Muga, C. Torres-Verdín, A. Mora, V. M. Calo, Simulation of wireline sonic logging measurements acquired with borehole-eccentered tools using a high-order adaptive finite-element method, J. Comput. Phys. 230 (16) (2011) 6320–6333.

[2] D. Pardo, P. Matuszyk, C. Torres-Verdin, A. Mora, I. Muga, V. Calo, Influence of borehole-eccentred tools on wireline and logging-while-drilling sonic logging measurements, Geophys. Prospect. 61 (s1) (2013) 268–283.

[3] C. Lu, Q. Liu, A three-dimensional dyadic Green's function for elastic waves in multilayer cylindrical structures, J. Acoust. Soc. Am. 98 (1995) 2825–2835.

[4] J. Rosenbaum, Synthetic microseismograms: logging in porous formations, Geophysics 39 (1) (1974) 14–32.

[5] L. Tsang, D. Rader, Numerical evaluation of the transient acoustic waveform due to a point source in a fluid-filled borehole, Geophysics 44 (10) (1979) 1706–1720.

[6] A. Kurkjian, Numerical computation of individual far-field arrivals excited by an acoustic source in a borehole, Geophysics 50 (5) (1985) 852–866.

[7] M. Bouchon, K. Aki, Discrete wave-number representation of seismic source wavefields, Bull. Seism. Soc. Am. 67 (2) (1977) 259–277.

[8] H. Leslie, C. Randall, Eccentric dipole sources in fluid-filled boreholes: Numerical and experimental results, J. Acoust. Soc. Am. 87 (6) (1990) 2405–2421.

[9] D. Schmitt, Dipole logging in cased boreholes, J. Acoust. Soc. Am. 93 (2) (1993) 640–657.

[10] T. W. Geerits, X. Tang, T. B. O. Hellwig, Multipole borehole acoustic theory: Source imbalances and the effects of an elastic logging tool, J Appl. Geophys. 70 (2) (2010) 113–143.

[11] M. Durán, R. Hein, J.-C. Nédélec, Computing numerically the Green's function of the half-plane Helmholtz operator with impedance boundary conditions, Numer. Math. 107 (2) (2007) 295–314.

[12] V. Laude, C. Jerez-Hanckes, S. Ballandras, Surface Green's function of a piezoelectric half-space, IEEE T. Ultrason. Ferr. 53 (2) (2006) 420–428.

[13] V.-S. Chan, L. Gray, T. Kaplan, G. Paulino, Green's function for a two-dimensional exponentially graded elastic medium, P. Roy. Soc. Lond A Mat. 460 (2004) 1689–1706.

[14] M. Durán, E. Godoy, J.-C. Nédélec, Computing Green's function of elasticity in a half-plane with impedance boundary condition, C.R. Acad. Sci. II B 334 (12) (2006) 725–731.

[15] J. Byun, M. Toksoz, Effects of an off-centered tool on dipole and quadrupole logging, Geophysics 71 (4) (2006) F91–F100.

[16] K. Graff, Wave Motion in Elastic Solids, Dover Publications, New York, 1991.

[17] M. Abramowitz, I. Stegun (Eds.), Handbook of mathematical functions with formulas, graphs, and mathematical tables, Dover Books on Mathematics, Dover, 1965.

[18] C. Pérez-Arancibia, M. Durán, On the Green's function for the Helmholtz operator in an impedance circular cylindrical waveguide, J. Comput. Appl. Math. 235 (1) (2010) 244–262.

[19] E. Kausel, Fundamental Solutions in Elastodynamics. A Compendium, Cambridge University Press, 2006.

[20] E. Peterson, Acoustic wave propagation along a fluid-filled cylinder, J. Appl. Phys. 45 (8) (1974) 3340–3350.

[21] X.-M. Tang, C. Cheng, Quantitative borehole acoustic methods, Vol. 24, Gulf Professional Publishing, 2004.

[22] W. Magnus, R. Soni, F. Oberhettinger, Formulas and theorems for the special functions of mathematical physics, Springer, 1966.

[23] A. Kurkjian, S.-K. Chang, Arrays of synthetic acoustic well logging waveforms: Computation and source design, IEEE T. Acoust. Speech 31 (4) (1983) 946–955.

[24] J. Ma, C. Torres-Verdín, Tool eccentricity effects on sonic waveforms acquired in deviated wells, slides of Presentation at the 12th Annual Meeting of the Consortium on Formation Evaluation, The University of Texas at Austin (Aug. 2012).